Quantitative measurement of the chemical composition of geological standards with a miniature laser ablation/ionization mass spectrometer designed for *in situ* application in space research

2016 Meas. Sci. Technol. 27 035904

(http://iopscience.iop.org/0957-0233/27/3/035904)

IOP Publishing Measurement Science and Technology
Meas. Sci. Technol. **27** (2016) 035904 (13pp) doi:10.1088/0957-0233/27/3/035904

Quantitative measurement of the chemical composition of geological standards with a miniature laser ablation/ionization mass spectrometer designed for *in situ* application in space research

M B Neuland[1], V Grimaudo[3], K Mezger[2], P Moreno-García[3], A Riedo[1], M Tulej[1] and P Wurz[1]

[1] Physics Institute, University of Bern, Space Research and Planetary Sciences, Sidlerstrasse 5, CH – 3012 Bern, Switzerland
[2] Institute of Geological Sciences, University of Bern, Baltzerstrasse 1+3, CH–3012 Bern, Switzerland
[3] Department of Chemistry and Biochemistry, University of Bern, Freiestrasse 3, CH–3012 Bern, Switzerland

E-mail: neuland@space.unibe.ch

Received 21 October 2015, revised 22 December 2015
Accepted for publication 18 January 2016
Published 2 February 2016

Abstract

A key interest of planetary space missions is the quantitative determination of the chemical composition of the planetary surface material. The chemical composition of surface material (minerals, rocks, soils) yields fundamental information that can be used to answer key scientific questions about the formation and evolution of the planetary body in particular and the Solar System in general. We present a miniature time-of-flight type laser ablation/ionization mass spectrometer (LMS) and demonstrate its capability in measuring the elemental and mineralogical composition of planetary surface samples quantitatively by using a femtosecond laser for ablation/ionization. The small size and weight of the LMS make it a remarkable tool for *in situ* chemical composition measurements in space research, convenient for operation on a lander or rover exploring a planetary surface. In the laboratory, we measured the chemical composition of four geological standard reference samples USGS AGV-2 Andesite, USGS SCo-l Cody Shale, NIST 97b Flint Clay and USGS QLO-1 Quartz Latite with LMS. These standard samples are used to determine the sensitivity factors of the instrument. One important result is that all sensitivity factors are close to 1. Additionally, it is observed that the sensitivity factor of an element depends on its electron configuration, hence on the electron work function and the elemental group in agreement with existing theory. Furthermore, the conformity of the sensitivity factors is supported by mineralogical analyses of the USGS SCo-l and the NIST 97b samples. With the four different reference samples, the consistency of the calibration factors can be demonstrated, which constitutes the fundamental basis for a standard-less measurement-technique for *in situ* quantitative chemical composition measurements on planetary surface.

Keywords: LIMS, chemical composition, space science, sensitivity, standard material, mineralogical analyses, planetary exploration

(Some figures may appear in colour only in the online journal)

1. Introduction

On every space mission to a planet, moon or asteroid, chemical composition measurements of rocks and soil on the planetary surface address many of the key scientific objectives. When employing a lander or rover, these measurements can be conducted *in situ* on the planetary surface. Such point source measurements are more sensitive and more detailed than measurements using a remote sensing instrument operating from orbit. Global compositional maps of a planetary body, recorded by orbiters, complement the high resolution measurements on the surface. Measuring the chemical composition of planetary material with a spatial resolution that is commensurate with the grain size of minerals in the rock yields information that otherwise is not accessible, e.g. rock constituents, mineralogy, or isotopic composition. Obtaining these data offers valuable clues to the origin of the planetary body, its formation and evolution [1]. Alternatively, chemical composition measurements of planetary material can be conducted in appropriate laboratory facilities only when the mission involves a sample return. Beside the fact that this involves a longer time of waiting for the data, sample return missions are costly in matters of the apparatus and risky relating to safe and contamination-free return to Earth.

Laser ionization ablation mass spectrometry (LIMS) is a well-established and widely used technique in numerous fields of research [2]. Fast progress in miniaturization of electronic devices and lasers to the point of micro-chip lasers allowed the development of very small and light weight LIMS instruments applicable for space research [3, 4]. Yet, the operation of laser ablation/ionization technique in space still is in its infancy and operation inflight still has to be demonstrated. However, numerous performance evaluations of miniaturized LIMS instruments in laboratories have demonstrated that this type of instrument is suitable for application in planetary space research [5, 6].

LIMS instruments have the positive benefit of being sensitive to all elements, however, sensitivity is not uniform. In terms of instrument and measurement simplification it is a considerable complication if a reference sample is needed for quantitative chemical composition measurements on a planetary surface. Hence, the characteristic set of relative sensitivity coefficients (RSCs) of a LIMS instrument necessarily needs to be determined carefully. With such a reproducible and robust calibration, the way is cleared for quantitative *in situ* chemical composition measurements in space. The approach of applying LIMS on a planetary surface would yield the portions of almost all elements with a very high spatial resolution, which is infeasible with, so far mostly applied, spectroscopic space instrumentation. High resolution chemical composition measurements for example allow the detection of micrometre-sized fossils preserved in minerals in planetary rocks [52] and hence the detection of past or present life.

This study reports experiments with the LMS instrument, a miniature laser ablation/ionization mass spectrometer, designed and built at the University of Bern [7]. To make this instrument a useful tool for quantitative chemical and isotopic analyses on planetary bodies, the RSCs for the rock-forming elements and a few minor and trace elements are derived.

It is now well established that the mineralogical endmembers of rocks and dust on the other rocky planets in the Solar System [8] as well as on exoplanets [9, 10] are similar to the ones on Earth. Four different natural terrestrial standard reference materials are used to study the LMS performance on these fine grained sabulous samples that are analogues for soils on an extraterrestrial planetary object. We measured the chemical composition of these samples with the LMS to determine the RSCs and to confirm their uniformity and reproducibility on different samples. The analytical measurements of these standards with LMS are a necessary step for going on from using LIMS methodology in the laboratory to an application in space exploration. Furthermore, the calibration measurements are conducive for the further development of the instrument as well as for narrowing down the technical specifications of a miniaturized LMS for a space mission.

2. Samples

All four rock standards are available from the National Institute of Standards and Technology (NIST) and the United States Geological Survey (USGS) in powdered form. To simplify handling of the samples, to guarantee a safe sample introduction and stable measurements by LMS and to protect the low pressure inside the LMS vacuum chamber, the powders were pressed to mechanically stable pellets. With a customized press, four pellets with diameter of 5 mm were produced. The pressure applied in the process was estimated using a force washer (HBM, KMR40kN). For each sample, the applied pressure, the pressing duration and the resulting pellet density are listed in table 1. The pressure uncertainty is estimated to be ± 30 MPa, resulting from the accuracy of the force washer calibration, and duration to be accurate to 5 s. The density error results from the measurements of the heights and weights of the pellets. In table 1 it can be seen that higher pressure and longer pressing time were needed for the production of a mechanically stable pellet from the USGS QLO-1 powder. This instance is most probably due to the chemical composition of the sample, hence minerals requiring higher pressure to reach the adhesion forces needed for pellet production.

The readily prepared pellet samples were placed on a steel sample holder inside four suitable holes, each 5 mm in diameter. The sample holder was labelled (figure 1) to prevent confusion of the similarly looking pellets: A = Andesite (USGS AGV-2), C = Cody Shale (USGS SCo-l), F = Flint Clay (NIST 97b), Q = Quartz Latite (USGS QLO-1). The four samples were investigated in LMS to derive the RSCs for such porous geological samples and to check conformity of the RSCs. Furthermore, these samples can be regarded as being good analogues for planetary material in general.

2.1. Andesite

The first Mars Pathfinder results identified the rocks in the landing site to be andesitic [11], though this finding was

Table 1. Powder samples investigated in this study, conditions of samples preparation and main constituents of the pellets.

Sample	Pressure (MPa)	Time (min)	Density (g cm^{-3})	Main constituents (wt%)
USGS AGV-2	220	5	1.79 ± 0.09	SiO_2 59.3 ± 0.7 Al_2O_3 16.9 ± 0.2
USGS SCo-1	280	10	1.93 ± 0.08	SiO_2 62.8 ± 0.7 Al_2O_3 13.7 ± 0.2
NIST 97b	280	5	2.20 ± 0.08	$Al_2Si_2O_5 > 95$
USGS QLO-1	700	60	1.65 ± 0.05	SiO_2 65.6 ± 0.5 Al_2O_3 16.2 ± 0.2

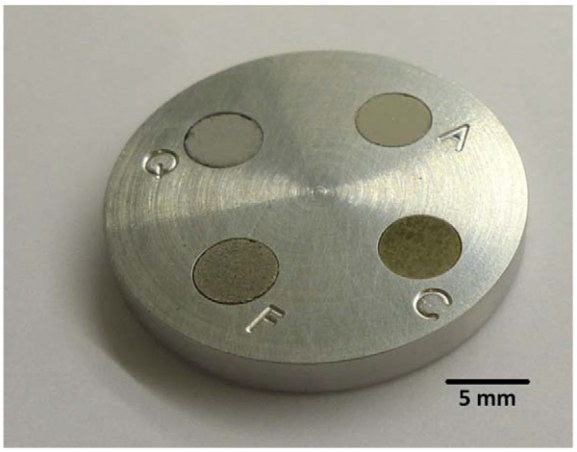

Figure 1. Sample holder assembled with the four standard samples USGS SCo-1 Cody Shale (C), NIST 97b Flint Clay (F), USGS QLO-1 Quartz Latite (Q) and USGS AGV-2 Andesite (A).

later revised, the Martian rocks being mostly basaltic [12]. Furthermore, andesites play a major role in the investigation of volcanism on planetary bodies and consequently the evolution of the early Solar System. The meteorite sample 'ALM-A', a fragment of the asteroid 2008 TC_3, is significantly richer in SiO_2, hence is more andesitic, than its companions, which are all ureilitic [13]. Hence, the conclusion can be drawn that silica-rich volcanism occurred on the parent body TC_3 [13, 14]. Similar results were reported for andesite in LL chondrites being an indicator for high-temperature events on the parent body, e.g. partial shock melting of the Itokawa asteroid [15].

2.2. Shale

Sedimentary rocks have been discovered by the Mars Science Laboratory Curiosity rover on the Martian surface at Yellowknife Bay, Gale Crater [16]. Hence, Cody Shale can serve as an analogue for rocks and soils on a planet, where liquid water is or was present.

2.3. Clay

Clay minerals have been found in many sites in the Solar System [17], e.g. on Mars [18], and they undoubtedly play an important role in connection with organic compounds [19].

2.4. Quartz latite

Latite is a felsic volcanic rock, defined as quartz latite, when containing more than 5% quartz. From spectral emissivity measurements of Mercury, latite is considered as one of the likely rock types on the Hermean surface [20]. Quartz discovered in meteorites gives information about the provenance of water in the Solar System [21]. In contrast to Earth, quartz was found on the Moon only in very small amounts [22].

These examples illustrate the significance of specific minerals and how they contain and retain information on the history of Solar System formation and evolution. Consequently, a scientific requirement for mass spectrometers being launched to space for operation on the surface of a planetary body is the capability for quantitative element composition measurements and mineralogical analyses. With the four pellet samples presented here, we demonstrate that LMS is a highly suitable instrument for such quantitative chemical composition measurements of rocks and soil in planetary exploration.

3. Experimental setup

The LMS instrument, a miniature laser ablation/ionization mass spectrometer coupled with a time-of-flight mass analyser, was designed and built at the University of Bern. All details about the LMS instrument are presented in previous publications and for this reason only a recapitulatory description of LMS will be given here. In-depth information is available in [5, 7, 23, 24].

The LMS (figure 2(a)) is operated at an ambient pressure in the 10^{-8} mbar range. A Ti − sapphire femtosecond laser (CPA, Clark-MXR Inc. USA) is used to ablate and ionize atoms from the sample surface. Laser key data are $\lambda = (775 \pm 5)$ nm, 190 fs pulse width, 1 kHz repetition rate, energy <1 mJ pulse^{-1}. Enabling experiments in a vast range of pulse energies and repetition rates, using this laser system offers the possibility for finding the optimum parameters for rocky and sabulous samples as they would be expected to be measured on a planetary surface. Operation of LMS in space is planned with a microchip laser, as presented in earlier LMS publications [7, 57]. Such miniaturized laser systems already today achieve a pulse width in the low ps range [58, 59] and intense research is ongoing.

The schematic in figure 2(b) indicates the pulsed laser beam, entering the instrument from the top and being focused onto the sample, which is placed under the instrument. Released ions enter the time-of-flight mass analyser. Mass separation occurs during passage through the field free drift tube. The ions are reflected back by the ion mirror, pass through the drift tube and reach the microchannel plate (MCP) detector (Chevron configuration). A circular multi-anode is used to collect the detector signal in up to four different channels with different gain factors [5], referred to as low gain (LG), medium gain (MG) and high gain (HG)

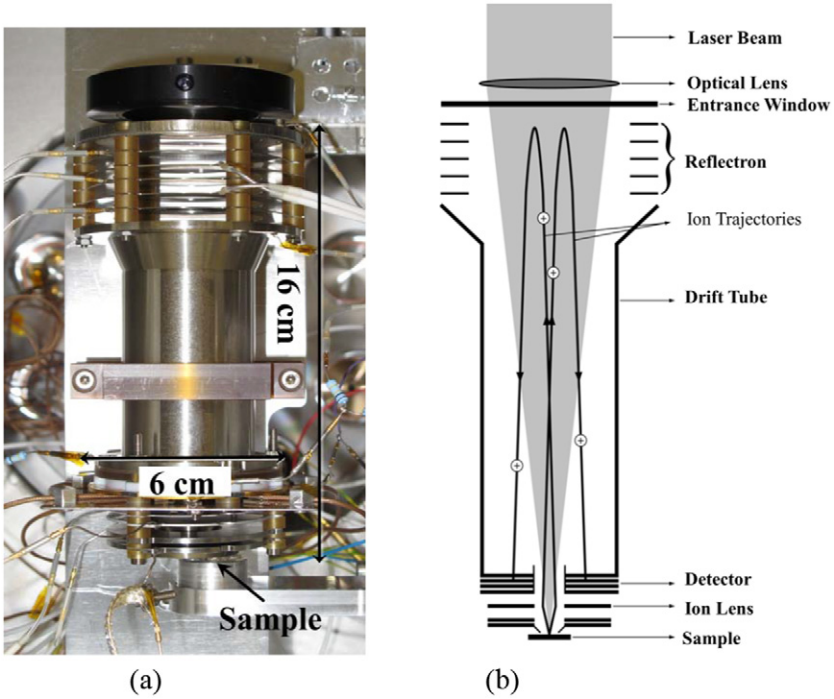

Figure 2. (a) The LMS instrument in the vacuum chamber. The small size of the instrument (Ø 60 mm × 160 mm) makes it suitable for operation in space exploration. (b) Schematic of the laser ablation mass spectrometer.

channels in the following. Data acquisition is rendered by two high speed ADC cards. Each laser pulse, hence each plasma plume from the sample surface, triggers the recording of a 20 μs long time-of-flight (TOF) spectrum, corresponding to a mass range of 1 to 600 u/e. The mass resolution of the LMS is typically $m/\Delta m = 200$–500 for element analysis of geological samples, but can be raised to $m/\Delta m \approx 850$ for isotope ratio measurements in a certain mass range [25] by adjusting the voltages applied to ion optics and detector and the distance between sample surface and LMS accordingly. This procedure amounts to a compromise between mass resolution and ion transmission hence signal intensity. To increase the signal intensity, usually multiple TOF spectra are summed up in the data analysis procedure, except for depth profiling studies, where single laser pulse spectra are analysed [26].

Inside the vacuum chamber, the sample is mounted on a microtranslational stage that allows accurate positioning of the desired analysis spot with an accuracy of 2 μm. Customized software makes it possible to define a template so that measurements in preselected patterns can be carried out fast and accurately.

LMS is a small (Ø 60 mm × 160 mm, figure 2(a)) and light-weight instrument. Including acquisition interfaces electronics and laser, the instrument weight is estimated to be approximately 2 kg and power consumption as low as 15 W [5]. These features result from LMS as an instrument being designed to operate on a planetary lander or rover.

4. Data collection

The chemical composition of the four geological standard reference samples (section 2) was measured with the LMS. Test measurements with different laser irradiances on the USGS SCo-l pellet resulted in best performance, regarding signal to noise ratio, signal intensity and mass resolution, when applying a laser fluence of 1.3 μJ pulse^{-1}, which is equal to an irradiance of 4.46 TW cm^{-2}. Consequently, this laser setting was used for all subsequent measurements. Preparatory data analysis of the test measurement showed that averaging of 10 single shot spectra is needed to obtain sufficient statistics and mass spectra of good quality in terms of white noise minimization. The averaging of TOF spectra is executed directly during the data acquisition procedure. Furthermore, the preparatory work showed that the first five spectra generally have to be discarded due to low intensity and asymmetrical shape of the mass peaks. This corresponds to the first 50 laser shots needed to remove the first surface layers and to form the initial crater on the sample. It was found that after ~270 laser shots intensity and mass resolution, hence spectrum quality, start to deteriorate, which can be ascribed to the ablation crater reaching a depth, where the ablation surface is out of the laser focus. Therefore, for each measurement position the data from 300 laser shots were recorded, but only data from shots 50 to 260 were used for data analyses. On each sample, a raster of 10 × 10 measurement points with 200 μm spacing from point to point was carried out and between 2 (USGS QLO-1) and 44 (USGS AGV-2) additional measurements were obtained for better statistics.

In previous experiments on two natural rock samples the craters generated by the laser ablation process were found to be approximately 15 μm in diameter after application of 2000 laser shots [27]. The powder samples in this study have lower densities than the rock samples investigated in [27], hence the ablation rate is assumed to be higher. However the number

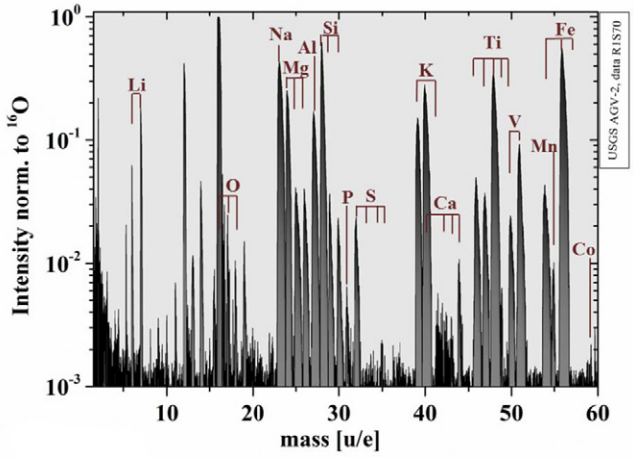

Figure 3. Typical mass spectrum (210 single laser shots) measured on the Andesite sample (USGS AGV-2). The intensity is normalized to ^{16}O, which represents the highest signal in the spectrum.

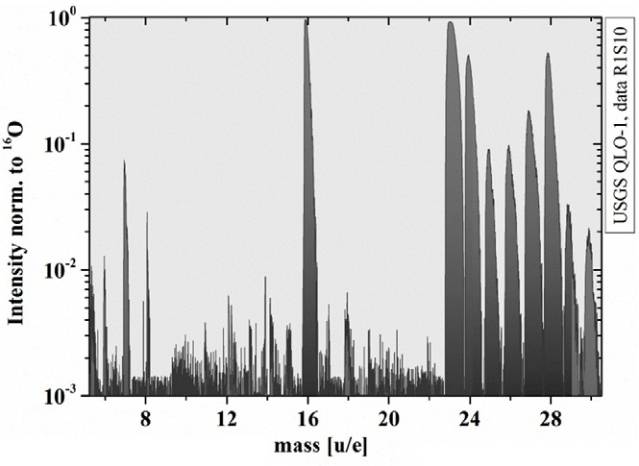

Figure 4. Mass spectrum of Quartz Latite (USGS QLO-1). The mass range from 5 to 30 u/e is displayed to illustrate the isotope ratios of Li, O, Mg and Si (table 2).

of laser pulses applied in one measurement is considerably smaller in this study than in [27]. Therefore the laser ablation craters on the pellet samples are assumed to have a similar depth and diameter as in [27].

Figure 3 shows a typical mass spectrum, measured on the Andesite (USGS AGV-2) pellet. The elements in the mass range of 1…60 u/e are assigned to the peaks. The intensities are normalized to the ^{16}O peak, which represents the highest signal in the mass spectrum. In addition, intensities are displayed in log-scale to enhance visibility of minor elements and isotopes. The spectrum was recorded in the HG channel, the channel exclusively used for the measurements here. Increasing the signal intensity by increasing detector supply voltage or laser irradiance yielded in a better signal also in the LG and MG channels (section 3), but in turn provoked a significant decrease of mass resolution, peak symmetry and detector performance. Hence, the data from LG and MG channels were used to ensure that individual peaks are not saturated, but these data were not included in the regular data analyses. The dynamic range of about three decades of the HG channel is sufficient in this case for analysis of the rock forming elements and several minor and trace elements. The mass resolution in this spectrum (figure 3, HG) is $m/\Delta m \sim 200 \pm 50$, which applies to all mass spectra included in this study.

Peaks that are saturated are not considered in the data analysis. The same applies to peaks that have isobaric interferences and peaks suffering from neighbouring high intensity peaks (an example is discussed below). To ensure exclusion of such data, the isotope ratios were checked for each element prior to data evaluation. The lower mass range of a typical mass spectrum (HG) of the Quartz Latite sample (USGS QLO-1) is displayed in figure 4, where some isotopes are seen as good examples. In table 2 the abundances of the Li, O, Mg and Si isotopes, derived from the mass spectrum (figure 4) are shown. Comparing the abundances, we find a good agreement of measured and known terrestrial values. Solely, the measured abundance of ^{24}Mg is lower than the terrestrial reference, which results in the isotopes ^{25}Mg and ^{26}Mg being

Table 2. The measured isotope ratios as derived from a mass spectrum of Quartz Latite (USGS QLO-1), figure 2. The reference values of terrestrial abundances are taken from [28].

	Relative isotope abundance (%)	
	Measured	Terrestrial
^{6}Li	8.64 ± 0.78	7.59
^{7}Li	91.36 ± 1.78	92.41
^{16}O	99.74 ± 0.02	99.757
^{17}O	0.04 ± 0.01	0.038
^{18}O	0.22 ± 0.02	0.205
^{24}Mg	74.83 ± 0.25	78.99
^{25}Mg	11.35 ± 0.15	10.00
^{26}Mg	13.82 ± 0.22	11.01
^{28}Si	92.70 ± 0.28	92.223
^{29}Si	4.34 ± 0.15	4.685
^{30}Si	2.96 ± 0.10	3.092

proportionally too abundant. The explanation for the problem with ^{24}Mg is the large signal of ^{23}Na increasing the baseline below the ^{24}Mg peak. The high signal of ^{23}Na results from the high abundance of Na in the sample and the high sensitivity of LMS to alkali metals (see section 5.1). The high signal causes the MCP detector reaching its limitations in matters of channel saturation and recharging, which can reduce the detection sensitivity for ions arriving at the detector directly after. Nevertheless, the effect is not severe here as attention was paid to not operating the detector in saturation regime. For the mass spectrum displayed in figure 4 it was verified by using the LG channel data that the peaks of ^{16}O and ^{23}Na are not saturated. For better visualization in the graph all intensities were normalized to the maximum intensity of ^{16}O.

Similar to this example, isotope ratios and saturation issues were carefully checked for all elements to ensure that only non-saturated peaks and peaks without isobaric interferences or free of overlap from adjacent peaks are taken for the subsequent analysis procedure. In the case of QLO-1, presented in figure 4 and table 2, the elemental content of Mg was derived

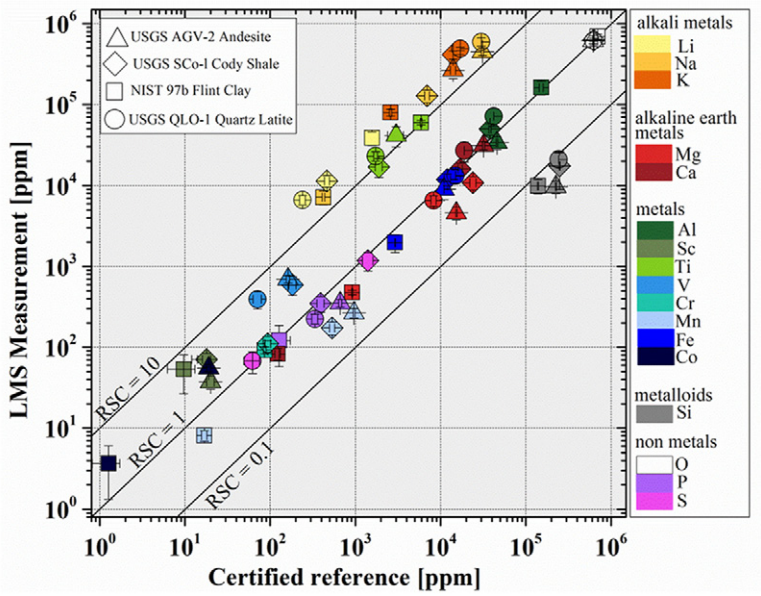

Figure 5. Comparison of measured versus certified abundance for the four different geological standard materials (see inset top left).

from the ^{25}Mg and ^{26}Mg isotopes assuming terrestrial isotopic abundances. In addition, this example shows that LMS is also a good instrument for isotope measurements. Furthermore, the example demonstrates that the accuracy for measurements of isotopic abundances is in the range of about 10%. In previous LMS publications it was demonstrated that highly accurate isotope measurements with an accuracy in the permill range can be performed with LMS [25], when settings are carefully adjusted to this mode. For the experiments presented here the instrument settings (ion optics voltages, laser irradiance) were not optimized for isotope measurements of one specific element, but for quantitative elemental measurements in a wide mass range, which is different from isotope measurements.

This study focuses on the elemental composition of the four standard reference samples (section 2). Therefore, in a first step, the isotopes that are categorized as unaffected by contamination, interference and saturation by checking isotope ratios are used to calculate the total abundance of the corresponding element assuming terrestrial isotopic abundances (taken from [28]). Subsequently, the measured peak areas of one element from all 100 (plus additional) measurements on one sample are merged in a histogram. A Gaussian fit is applied to the histogram and the centre of the Gaussian distribution gives the result for the measured content of the element in the corresponding reference sample. The Gaussian fit has the advantage that single outlier measurements, which show a significantly higher or lower intensity than all the others, do not affect the result too much. Such effects are presumably caused by irregularities in the homogeneity of the powder sample and localized matrix effects. The laser performance itself can be considered as an unlikely reason for such variations as the fluctuations of the laser irradiance are known to be stable in the permill-range [29]. However, only few mass spectra showed such differences. As an example, neglecting all mass spectra where an element value deviated more than 2σ from the Gaussian centre, resulted in 85 useful measurements (USGS SCo-l) for further data evaluation, e.g. for mineralogical analyses (section 5.2), from originally 104 measurements.

5. Results and discussion

5.1. Relative sensitivity coefficients

LIMS instruments are, like most other analytical instruments, not uniformly sensitive to all elements. The variable elemental sensitivity is caused by the different physical properties of the elements. Hence, a determination of the relative sensitivity coefficient (RSC) of each element is essential for quantitative chemical composition measurements with a LIMS instrument. The RSCs comprise the efficiency of atomization and ionization of the sample material. In a previous publication it was shown that the RSCs are closer to 1, i.e. the mass spectra express more directly the true chemical composition of the sample, when fs-laser pulses are used compared to an earlier LMS setup, where a ns-laser system was applied as an ion source [29]. Similar findings are also reported by other groups [30].

The RSCs are calculated as the ratio of the measured elemental abundance, determined by experiment, and the certified value. The measurements performed with LMS yield the areas of the peaks in the mass spectrum, respectively, after conversion of the isotope areas, to the area of the corresponding element (section 4). This value is set into relation to the certified element abundance. For each element, this coefficient is divided by the coefficient of oxygen, which is determined similarly. Oxygen is the most abundant element in the four investigated samples (table 1). Hence, the RSC is calculated as

$$\mathrm{RSC_i} = \frac{A_i^{\mathrm{exp}}}{A_{\mathrm{O}}^{\mathrm{exp}}} \Big/ \frac{A_{\mathrm{i}}^{\mathrm{ref}}}{A_{\mathrm{O}}^{\mathrm{ref}}}, \qquad (1)$$

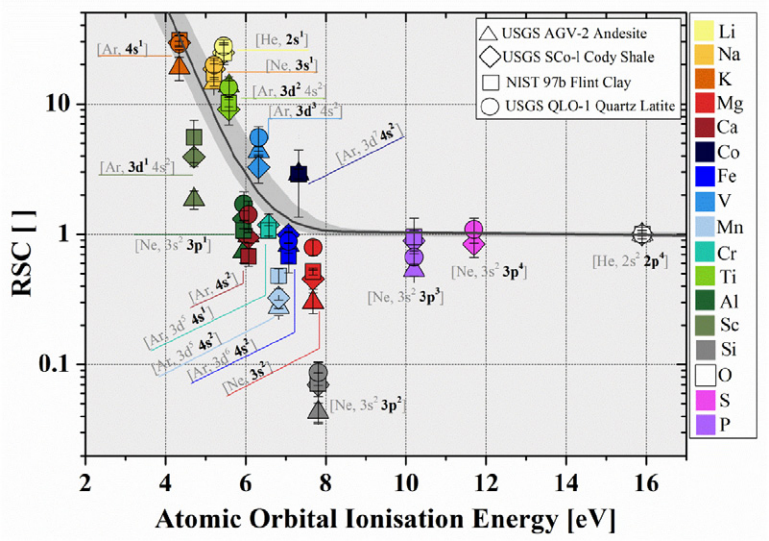

Figure 6. The RSCs plotted against the atomic orbital ionization energy, from [40]. The electron configuration of each element is given next to the data points with the orbital, from which ionization takes place marked in bold letters. The curve designates the least square fit of the averaged RSCs to equation (2) (from [38]).

where A_i^{exp} is the average peak area of element i, resulting from the statistical analysis of about 100 measurements of this species on the sample. Accordingly, A_i^{ref} is the certified reference mean value for the investigated sample and the similar notation used for oxygen. The uncertainty of the calculated RSC value results from the errors of peak integration and background subtraction and from the standard error of the mean of the Gaussian fit for determination of the abundance of the corresponding element.

In figure 5 the comparison between the measured and the certified values is presented. The LMS measurements are displayed as a function of the reference values with the elements color-coded and the four different samples represented by different symbols (see inset figure 5, top left). The diagonal line specifies the optimal case of all RSCs being equal to 1. Hence, in figure 5, the distance of a data point to the unity-RSC-line, measured perpendicularly, represents the absolute value of the RSC of the element. The lines parallel to the diagonal illustrate RSCs one order higher and lower, according to the labels.

For all four samples, the RSCs of Li, Na and K are larger than 1, meaning that their abundances appear higher in the measured spectra compared to their actual abundance in the sample. This is due to the low first ionization potential of these elements, which is $\lesssim$5 eV for Li, Na and K [28], and hence, in comparison to other element groups, the alkalis are efficiently ionized. The RSCs of metals, alkaline earth metals and non-metals, included in the analysis, are close to one, with the exception of Ti and Si, which are markedly higher and lower, respectively. Moreover, it can be seen from figure 5 that Sc, Co and V have RSCs larger than 1 as well, even though less distinctive.

The low sensitivity of LMS to Si, respectively the small RSC, was discussed as well in earlier publications on LMS, where a ns-laser (Nd:YAG) was applied for ablation/ionization. The Nd:YAG laser only allows irradiances below 1 GW cm^{-2} and due to the longer pulse duration, interaction with the sample material is of different nature, regarding the absorption by the crystal lattice, thermal effects and other parameters. Operating the ns-laser in IR-regime a $\mathrm{RSC_{Si}} = 0.007$ was reported [23] and $\mathrm{RSC_{Si}} = 0.0003$, when using a wavelength in the UV range [31]. In these cases the high evaporation temperature of Si, as well as the high ionization potential, were the evident explanation for the low sensitivity to Si. Operating the LMS with the fs-laser, the thermal material properties are not important anymore as the interaction of the fs-laser with the sample material happens on timescales that are shorter than the lattice relaxation time [32] and the heat conduction of the solid [33]. Consequently, the energy transfer from photons to the atoms of the sample is controlled by dielectric, hence energetic interactions, when a fs-laser is used as an ablation source [34–36], in contrast to the ns laser ablation, where a strong dependence on thermal effects is observed [37, 38].

For the analysis of the dependence of the RSCs on physical parameters of the different elements, we investigated the RSCs as a function of the heat of vaporization, the enthalpy of atomization, the electronegativity, the energy of first and second ionization, the first ionization time, the work function and the Fermi energy. A correlation of the RSCs with thermal properties, ionization time and energy of second ionization was not observed, but with increasing electronegativity, increasing first ionization and Fermi energy as well as with increasing work function, the RSCs show a decreasing trend. This likewise correlation to all the latter parameters is plausible as they are related quantities [39], e.g. for metals the work function equals the level of first ionization. Our measurements affirm the independence of the RSCs from any kind of thermal physical parameters. We investigated the RSC values of the elements as a function of thermal conductivity, condensation and evaporation temperature, heat of fusion and heat of vaporization of the elements and no definite correlation was observed.

As the ionization level is a parameter defined for all elements that are included in this study (contrary to the Fermi energy) we present the RSCs as a function of the energy of first

ionization, more precisely the atomic orbital ionization energy (from [40]). The results are shown in figure 6, where the data points of each element are labelled with the electron configuration and the orbital, from which the electron is released, marked in bold font. Congruently to figure 5, it can be seen that many RSCs of the elements included in this analysis are close to 1 with moderate variability for the RSCs derived from different samples. For completeness, the corresponding graph for the Fermi energy is shown in the appendix, figure A1.

Figure 6 shows the RSC values as a function of atomic orbital ionization energy. Most of the RSCs are located at the RSC = 1 line, but the RSCs of Li, Na and K are distinctly larger than 1. The efficient ionization of alkali metals can be assigned to the ionization from the half-filled s-orbital, which requires very little energy (~ 4–5 eV), as already noted before.

Ti, Sc and V also have RSCs larger than 1 as well (see figures 5 and 6). Although the latter elements possess 4s-electrons (electron configuration shown in figure 6) the ionization takes place from the favourable uncompleted 3d-orbital. For example ionization of Sc from the 4s-orbital would require 1 eV more than from the 3d-orbital [40].

For the elements, where ionization takes place from a completed or half-completed s-orbital and/or the d-orbital of the second outer shell is not full (Mg, Ca, Mn, Cr, Fe and Co), the RSCs are close to 1 with the exception of Co. A Co atom is not ionized by removing an electron from the 3d-, but from the completed 4s-orbital, similarly to Fe. Ionization requires ~7 eV for both elements. In spite of these similarities, RSC_{Co} is > 1, while RSC_{Fe} is $\lesssim 1$. But respecting that the investigated samples contain only low concentrations of Co, the relative error increases. Based on the reference data, the NIST 97b sample only contains (1.27 ± 0.45) ppm of Co. The LMS measurement resulted in (3.68 ± 2.35) ppm Co, which gives $RSC_{Co} = 2.90 \pm 1.54$ (figures 5 and 6). Hence, this relative error of 53% of the RSC_{Co} results from the measurement error that comprises the error of peak integration and background subtraction. Naturally these errors are larger, in a relative sense, for peaks with smaller signal to noise ratios. Additionally, the error of the certified reference value (figure 5) adds to the uncertainty of the RSCs. Respecting the large error of RSC_{Co}, it is compatible with RSC ≈ 1 like Fe.

The non-metals O, P and S require higher energies for ionization ($\geqslant$10 eV) than the metals. Ionization of these non-metals takes place from partly filled p-orbitals and the RSCs are all very close to 1 or $\lesssim 1$ (figure 6). Aluminium, though being a metal and having an ionization energy of ~6 eV, complements this group.

In comparison to the other elements included in this analysis, the sensitivity of LMS to Si is very low. For all four investigated samples the measured RSC_{Si} is < 0.1 for the LMS instrument. It is important to recall that the atomic orbital ionization energy, hence the electron configuration of an element, certainly does play a role in the process of laser-matter interaction, as demonstrated by the correlation of RSCs to orbital ionization energy (figure 6), but that numerous different effects add to the ablation/ionization process to a significant extent. A substantial influence on the ablation process is attributed to matrix effects [30]. $(SiO_4)^{4-}$ crystals are the major host for Si in the four investigated samples (see table 1). With a bond dissociation energy of 8.27 eV [41], the Si–O bond is significantly more stable than the binding of O to the metals. For example, the dissociation energy of Al–O is 5.31 eV and only 4.24 eV are required for dissociation of the Fe–O bond [41].

Furthermore, the wavelength of the used laser ion source influences the ablation process [42, 43], albeit for fs-laser ablation the dependence is reported to be rather moderate [32, 44]. However, the wavelength of (775 ± 5) nm, used in this study, corresponds to a photon energy E_γ of about 1.6 eV. As the photon density in the laser pulses is high enough, elements requiring energies higher than E_γ for ionization are getting ablated and ionized as well. As expected, the probability for multi-photon processes is significantly higher for ablation/ionization the lower the number of needed photons is, in agreement with the data displayed in figure 6.

Reducing the wavelength, hence increasing E_γ (300 nm $\Rightarrow E_\gamma \approx 4.1$ eV, for example), could, when keeping the photon density the same, result in less intense element fractionation. This statement is based on the consideration that, when increasing the photon energy, higher ionization or bond dissociation energies would be accomplished by smaller numbers of photons. Assuming the probability for single photon events remaining constant, increasing the photon energy would result in an increase of the RSCs specifically of those elements that have very small RSCs due to the high ionization or bond dissociation energy, e.g. Si. In summary this means that a shorter wavelength could reduce the variability of RSCs for different elements.

In Zhang *et al* 2015 [38] the authors present a model comprising various physical parameters of the elements as well as of the ablation and ionization process itself, from which they derive a theoretical estimate for the RSCs as a function of the plasma temperature T, the potential of first ionization IP and the electron number density N_e. Taking into account that in [38] the RSCs were calculated in reference to Fe and not to O (see equation (1)), the formula was adopted from [38] as

$$\mathrm{RSC}_i = \frac{N_e \cdot \left(\frac{h^2}{2\pi\, m_e k_B T}\right)^{\frac{3}{2}} \exp\left(\frac{-\mathrm{IP}_i}{k_B T}\right) + 1}{N_e \cdot \left(\frac{h^2}{2\pi\, m_e k_B T}\right)^{\frac{3}{2}} \exp\left(\frac{-\mathrm{IP}_{Ox}}{k_B T}\right) + 1}, \qquad (2)$$

with the ionization energy of oxygen $\mathrm{IP}_{Ox} = 15.9$ eV [40]. Inserting for each element i the values of the atomic orbital ionization energy (figure 6) and the averaged value of the RSCs from the four different samples, we find the fit parameters $N_e = 5.80 \times 10^{25}$ cm^{-3}, $T = 6889$ K. The RSC of Si was excluded from the curve fit, as this element is considered to be a special case due to its strong Si–O bonds in the $(SiO_4)^{4-}$ tetrahedra in minerals.

The fit of equation (2) to the data is plotted to figure 6 as a line. The shaded area around the curve equals the range of the fit parameters that are the results from fitting equation (2) to the RSCs of each single sample. The fit parameters N_e and T for the individual samples can be found in the appendix in the two last lines of table A1. Except the special case of Si,

most of the RSCs conform well to the theoretical function from [38] within the given uncertainty ranges. Deviation from the theoretical RSC values of a few elements, like Mg or Mn, is attributed to matrix effects, binding energy of the elements in the mineral or specific effects that influence the ablation and ionization processes under fs-laser application, e.g. reflectivity of the sample surface.

Although the RSCs, resulting from the investigation of the four different geological powder pellets, are not all exactly 1, this is not a constraint for quantitative chemical composition measurements. If the RSCs of a LIMS instrument are established by prior measurements of reference samples, the analyses of mass spectra are quantitative and informative in every respect [31].

Figure 5 shows that the resulting RSC of each element is similar within the range of uncertainty (see figure 6, *y*-error bars) for all different sample matrices although the detailed chemical composition of the four geological standard references is different. In more specific terms this means that the LMS sensitivity for an element is independent of its abundance in the sample. For example, the abundance of Na ranges from (422 ± 14) ppm in the NIST SRM 97b over (6934 ± 462) ppm in the USGS SCo-l to $(30\,000 \pm 1000)$ ppm in the USGS AGV- 2 and the QLO - 1 sample. The resulting average RSC for Na is 17.50 with a root mean square deviation of 23%. Such scattering of the RSC for one element determined from measurements of different samples could be ascribed to different matrix effects such as the crystal structure that is the host of the element to be analysed and its orientation [45]. However, when carrying out chemical composition measurements of powder samples with LMS, this effect is considered to be of minor importance as crystal orientations will be random in a powder.

Additionally, regarding the RSC errors, it has to be taken into account that also the reference values of elemental abundances of the natural standards (equation (1) A^{ref}) are given with a non-negligible uncertainty. Relative errors of individual elements from the references are, for example, as large as 35% each for Sc, Co and P in the NIST 97b or 20% for Ti in the AGV-2 sample (see figure 5, *x*-error bars). Complying with error propagation of equation (1), these uncertainties contribute to the errors of the resulting RSCs as well. Elements that show larger uncertainties of the reference concentrations (figure 5, *x*-error bars) have accordingly larger RSC errors (figure 6, *y*-error bars).

Furthermore, the measured elemental content (equation (1), A^{exp}) contributes to the RSC error. Background subtraction, delimitation and integration of the single isotope peaks in the measured mass spectra yield a statistical error. Hence, the resulting peak area correspondent to the element, determined by the Gaussian fit, is affected by a statistical error, which is about 5%–10%.

Including all the errors mentioned, this leads to a measurement precision of about 25% for elemental abundances. RSCs could be narrowed down only by increasing statistics, thus measurements on other reference materials. Yet, the RSC allocation including the results from four samples is sufficient for elemental analysis (section 5.2).

5.2. Mineralogy

Measurements of the chemical composition of a rock or soil sample, performed for example on a planetary surface, allow direct conclusions about the normative mineralogy of the material. Information about minerals on a planetary surface and subsurface offers valuable clues to the conditions, under which the material formed, e.g. pressure, temperature or environmental factors like the presence of water.

We carried out a first step mineralogical analysis using as an example Cody Shale (USGS SCo-l, see section 2) and investigated the ratios of the main rock-forming elements Si, Ca and Al. The abundances were corrected for LMS sensitivity using the respective RSCs. In section 5.1 it was shown that the mass spectrometric analysis of LMS measurements carried out on four different samples (table 1) results in basically identical sets of RSCs (table A1). Consequently, for the chemical analysis of Cody Shale, the average RSC values from this study were applied, which are $\mathrm{RSC_{Si}} = 0.07 \pm 0.01$, $\mathrm{RSC_{Al}} = 1.2 \pm 0.11$ and $\mathrm{RSC_{Ca}} = 1.00 \pm 0.11$. The results are shown in a ternary diagram in figure 7(a) with the potential modal minerals indicated. The errors of the fractions of Si, Ca and Al are $\pm$ 0.10,$\pm$ 0.05 and $\pm$ 0.08 respectively. The shaded areas in the graph mark the ratios of minerals that are, based on [46], contained in the sample. These areas were enlarged according to the errors of the data points.

The bulk Al–Ca–Si-composition of USGS SCo-l, determined from the material data sheet, is closest to pure quartz. It is marked by a red dot in figure 7(a). Most of the measured compositions are close to pure SiO_2, hence quartz, scattering around the bulk composition. In addition to the bulk composition, mineral compositions are marked and labelled in figure 7(a). A couple of data points accumulates at the element ratios Si : Al = 1 : 1 and Si : Al = 3 : 1. These ratios can be assigned to pure kaolinite, illite, albite plagioclase and K-feldspar. Six measurements, containing mostly Ca, can be identified as dolomite. Data points representing compositions that are not in the range of a pure mineral can be identified as mixtures of these minerals. Due to the grain sizes of the minerals that range from 2 to 50 μm [46] it is expected that many measurements will contain mixtures of different mineral grains, as the LMS laser spot is approximately 15 μm in diameter (see section 3). Nevertheless, this example demonstrates that this diameter of the laser focus is sufficient to resolve single mineral grains. For the detailed mineralogical composition of the SCo-1 sample, the reader is referred to table A2 in the appendix, where the literature values (from [46]) are reproduced together with the mineral formulae (from [47]).

In figure 7(b) the similar ternary diagram is presented for the NIST 97b sample. The red dot marks the bulk composition of the Flint Clay as it results from the numbers given in the data sheet of the standard reference material. The NIST 97b sample consists mainly of the mineral kaolinite, compare also to figure 7(a), which is in agreement with an earlier report [48]. Equally to the ternary diagram of SCo-1 (figure 7(a)), the averaged RSC values of Ca, Al and Si were applied to the

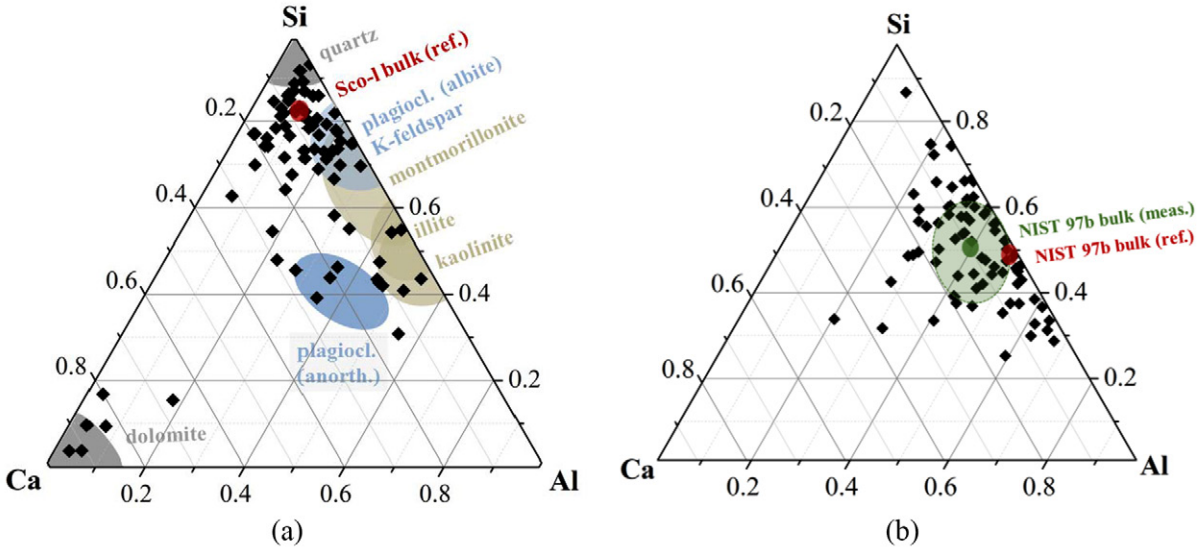

Figure 7. Ternary diagrams illustrating the mineral components of the Cody Shale (a) and the Flint Clay (b) sample. The diagrams comprise the LMS measurements with the averaged RSCs applied (black diamonds). The bulk composition, displayed by a red dot in both graphs, is derived from element values given in the data sheets accompanying the reference materials. Additionally, shaded areas mark the minerals that are, based on reference [46], contained in the sample (a). Further explanation in the text.

LMS data. The measured bulk composition is marked in the graph by a green point. The distance between the measured and the reference bulk composition demonstrates the effect of applying the averaged RSC values instead of the RSC values that were explicitly determined for the NIST 97b sample (see table A1). However, the literature bulk composition is included in the range of uncertainty of the measured bulk composition, which is designated by the shaded area. In detail, these uncertainties of the measured element ratios are ± 0.1 for Si, ± 0.05 for Al and ± 0.1 for Ca.

In figure 7(b) the data points scatter around the bulk composition with no explicit accumulation of data points apart from that. This is likely caused by the fine grained nature of the NIST 97b sample [48] and hence, each LMS measurement is a mixture of different minerals. The LMS measurements support the claimed homogeneity of the sample, meaning that the bulk composition is valid also for small scales down to ~10 μm, thus confirming the capability of the LMS for quantitative measurements. The result shows that the statistics of the measurement (~100 measurement points) is sufficient for an estimation of the bulk sample composition and that furthermore the chosen statistics for single mass spectra (300 laser shots per position) is suitably selected for this type of sample. In summary, this means that with LMS a bulk measurement can be carried out within only about 5 min. This aspect is of importance for an LMS instrument operating in space, where measurement time is valuable in terms of power consumption.

6. Conclusion

We measured the chemical composition of four geological standard samples with a miniature laser ablation/ionization mass spectrometer. From the measured elemental abundances, the RSCs of 17 elements were derived. An ideal LIMS instrument would exhibit the property of having similar sensitivity for all elements, hence having all RSCs equal to 1, which is precluded by the different physical properties of the different elements. However, having a stable set of RSCs derived from reference samples, quantitative chemical composition measurements can be carried out, which are the basis for various following analyses.

Almost all of the RSCs that were derived from the measurements are close to 1 (figure 5) and the RSCs for individual elements, derived from different samples, conform within the limits of the given uncertainties (figure 5, table A1). The dependence of the RSCs on different physical parameters was investigated. In accordance with preceding research, a correlation of the RSCs with parameters of the elements that are representative in thermal processes was not observed. On the contrary, concordant dependence of the RSCs on atomic energetic parameters was found. These findings are in agreement with the intense research on fs-laser ablation reported in [32, 37, 44, 49–51].

Beside a decreasing trend of the RSCs with increasing work function, ionization energy and Fermi energy (figure A1), the RSC values could be attributed to the electron configuration of the elements (figure 6, table A1). Thus, the electron configuration is linked to the ionization energy, which is connected to the Fermi energy and the work function. However, the light metals Ti, Sc and Al possess similar ionization energies (~5–6 eV), but the LMS sensitivity for Al was measured to be distinctly smaller than for Ti and Sc. From the electronic configuration of these elements, we conclude that this finding is attributed to Al being ionized from a p-orbital, while for Ti and Sc the ionizing electron is extracted from a d-orbital. We suppose that this correlation can be caused by the directionality of the different orbitals, hence the probability of the direction matching with impacting photons.

Using the examples of Cody Shale and Flint Clay it could be shown that the LMS data quality is well suited for chemical and mineralogical analyses. The RSCs that were applied in these analyses are the averaged values from all four standard samples. The resulting ternary diagrams (figure 7) are in good

agreement with the quoted mineralogical compositions of the sample (table A2). These examples demonstrate the robustness of the determined RSC set as well as the capacity of the LMS instrument to infer the normative mineralogy. This study shows that such a set of RSCs is applicable to a diversity of geological samples that have a similar texture/grain size. It has to be investigated to what extent the same RSCs can be used for chemical composition measurements of rock samples or individual mineral grains under same conditions.

The LMS is designed for application in space research and planetary exploration. The instrument is light-weight and has a low power consumption [5]. When operated on a lander or rover on a planetary surface, LMS could contribute eminently to the exploration of the planetary surface [4, 31, 52] and subsurface [26].

Acknowledgments

This work is supported by the Swiss National Science Foundation (SNF).We further acknowledge the work of the mechanical workshop of the Physics Institute, University of Bern. In particular we thank Beat Käser for manufacture of the labelled sample holder and the pellet press.

Appendix

Table A1. RSCs determined by measurements on four different geological samples (columns). For elements (rows) no RSC value given, no certified abundance was provided in the material data sheet. The last column contains the similarities as stated in the main text, the approximate Fermi energy E_F and the electron configuration with the orbital that gets subducted an electron upon ionization marked in bold letters. X stands for an integer 1…7, depending on the specific element (compare figure 6), ng = noble gas. In the last lines the results for electron number density and plasma temperature are listed. These result from the fit of the RSCs to equation 2.

Sample element	USGS AGV-2 Andesite	USGS SCo-l cody shale	NIST 97b flint clay	USGS QLO-1 quartz latite	Comment
Li	——	24.73 ± 3.74	24.69 ± 4.80	27.76 ± 3.13	Alkali metals [ng, $\mathbf{Xs^1}$] $E_F \leqslant 5$ eV
Na	14.52 ± 1.46	18.51 ± 3.11	17.02 ± 3.28	19.94 ± 2.49	
K	18.97 ± 3.89	29.56 ± 3.52	30.80 ± 2.73	28.86 ± 1.43	
Mg	0.30 ± 0.05	0.45 ± 0.08	0.52 ± 0.33	0.79 ± 0.11	Alkaline E. Metals [ng, $\mathbf{Xs^2}$] $E_F \approx 5…7$ eV
Ca	0.97 ± 0.11	0.94 ± 0.16	0.68 ± 0.11	1.42 ± 0.38	
Mn	0.27 ± 0.04	0.32 ± 0.06	0.48 ± 0.06	——	Metals [ng, $3d^x$, $\mathbf{4s^x}$] $E_F \approx 10…12$ eV
Cr	——	1.18 ± 0.25	1.07 ± 0.10	——	
Fe	0.82 ± 0.21	0.99 ± 0.14	0.68 ± 0.17	0.89 ± 0.17	
Co	2.91 ± 0.25	——	2.90 ± 1.54	——	
Ti	13.74 ± 2.49	9.08 ± 2.20	10.14 ± 0.66	13.40 ± 1.66	(light) metals [ng, $\mathbf{3d^x}$, $4s^2$] $E_F \approx 8…10$ eV
Sc	1.86 ± 0.29	3.92 ± 0.61	5.53 ± 1.97	——	
V	4.31 ± 0.37	3.26 ± 0.79	——	5.53 ± 1.17	
Al	0.73 ± 0.13	1.00 ± 0.13	0.99 ± 0.18	0.73 ± 0.18	
O	1.00 ± 0.08	1.00 ± 0.13	1.00 ± 0.07	1.00 ± 0.03	[ng, Xs^2, $\mathbf{Xp^x}$] non-metals
P	0.53 ± 0.05	0.89 ± 0.18	0.95 ± 0.37	0.67 ± 0.08	
S	——	0.84 ± 0.18	——	1.09 ± 0.24	
Si	0.04 ± 0.01	0.07 ± 0.03	0.07 ± 0.01	0.09 ± 0.02	metalloid $E_F \approx 12.5$ eV
Fit parameters (equation (2))					
N_e (10^{25} cm^{-3})	2.09	10.9	24.90	4.70	
T (10^3 K)	7.28	6.31	5.75	7.81	

Table A2. Reference mineralogical composition of USGS SCo-l. in vol% [46]. Using the mineral densities given in [47] and [53] and mol masses (from [28], the vol% were converted to atomic fraction (0.1 atom% ≙ 1000 ppm) with the assumption that 6% plagioclase correspond to 3% albite and 3% anorthite and that 40% mixed clay minerals consist of 30% illite- and 10% montmorillonite-like clays.

Mineral	Empirical formula [47]	vol%	atom%
Quartz	SiO_2	29	68
Dolomite	$CaMg[CO_3]_2$	6	5
Plagioclase		6	
	$NaAlSi_3O_8$ (albite)		1.5
	$CaAl_2Si_2O_8$ (anorthite)		1.5
K − feldspar	$KAlSi_3O_8$	1	0.5
Kaolinite	$Al_2Si_2O_5(OH)_4$	5	3
Illite	$K_{0.65}Al_2Al_{0.65}Si_{3.35}O_{10}(OH)_2$	10	4
Mixed clay minerals		40	
¾ illite-like	see above		11
⅔ montmorillonite-like	$(K,Na)_{0.35}(Al,Mg,Fe)_{2\text{-}3}Si_{3.65}Al_{0.35}O_{10}(OH)_2 4H_2O$		2

Note: + chlorite (2 Vol.%) + pyrite, apatite, gypsum (below detection limit).

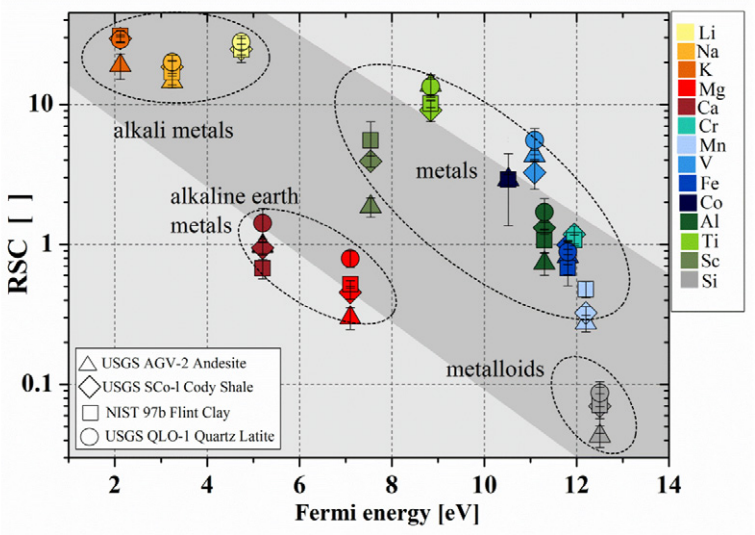

Figure A1. The RSCs as a function of the Fermi energy (from [54]). Data of O, P and S are not displayed in this plot, because the Fermi level is only a defined physical variable for metals and semiconductors.

References

[1] McSween H J and Huss G 2010 *Cosmochemistry* (Cambridge: Cambridge University Press)

[2] Lin Y, Hang W and Huang B 2010 Progress of laser ionization mass spectrometry for elemental analysis—a review of the past decade *Spectrochim. Acta* B **65** 871–83

[3] Brinkerhoff W 2005 On the possible in situ elemental analysis of small bodies with laser ablation TOF-MS *Planet. Space Sci.* **53** 817–38

[4] Wurz P, Whitby J and Managadze G 2009 Laser mass spectrometry in planetary science *Future Perspectives of Space Plasma and Particle Instrumentation and International Collaborations* American Institute of Physics *AIP Conf. Proc.* **CP1144** 70–5

[5] Riedo A, Bieler A, Neuland M, Tulej M and Wurz P 2013 Performance evaluation of a miniature laser ablation time-of-flight mass spectrometer designed for *in situ* investigations in planetary space research *J. Mass Spectrom.* **48** 1–15

[6] Managadze G, Wurz P, Sagdeev R, Chumikov A, Tuley M, Yakovleva M, Managadze N and Bondarenko A 2010 Study of the main geochemical characteristics of phobos' regolith using laser time-of-flight mass spectrometry *Sol. Syst. Res.* **44** 376–84

[7] Rohner U, Whitby J and Wurz P 2003 A miniature laser ablation time-of-flight mass spectrometer for *in situ* planetary exploration *Meas. Sci. Technol.* **14** 2159–64

[8] Vaniman D *et al* 2014 Mineralogy of a mudstone at Yellowknife Bay, Gale Crater, Mars *Science* **343** 6169

[9] Duffy T, Madhusudhan N and Lee K 2015 Mineralogy of super-earth planets *Treatise on Geophysics* 2nd edn (Oxford: Oxford University Press) pp 161–72

[10] Pagano M, Truitt A, Young P and Shim S 2015 The chemical composition of t ceti and possible effects on terrestrial planets *Astrophys. J.* **803** 90–6

[11] Rieder R, Economou T, Wänke H, Turkevich A, Crisp J, Brückner J, Dreibus G and McSween H Jr 1997 The chemical composition of Martian soiland rocks returned by the mobile alpha proton x-ray spectrometer: preliminary results from the x-ray mode *Science* **278** 1771–4

[12] McSween H Jr, Taylor G and Wyatt M 2009 Elemental composition of the Martian crust *Science* **324** 736–9

[13] Bischoff A, Horstmann M, Barratt J, Chaussidon M, Pack A, Herwartz D, Ward D, Vollmer C and Decker S 2014 Trachyandesitic volcanismin the early Solar System *Proc. Natl Acad. Sci. USA* **111** 12689–92

[14] Goodrich C, Hartmann W, O'Brian D P, Weidenschilling S, Wilson L, Michel P and Jutzi M 2015 Origin and history of ureilitic material in the solar system: The view from asteroid 2008TC3 and the Almahata Sitta meteorite *Meteor. Planet. Sci.* **50** 782–809

[15] Takeda H, Nagaoka H, Yamaguchi A, Karouji Y and Yazawa Y 2015 Mineralogy of some evolved LL chondrites with reference to asteroid materials and solar system evolution *Earth, Planets Space* **67** 5

[16] McLennan S and MSL Science Team *et al* 2014 Elemental geochemistry of sedimentary rocks at Yellowknife Bay, Gale Crater, Mars *Science* **343** 1–10

[17] Cairns-Smith A and Hartmann H 1986 *Clays in the Solar System Clay Minerals and the Origin of Life* (Cambridge: Cambridge University Press) ch 6 pp 105–29

[18] Bristow T F *et al* 2015 The origin and implications of clay minerals from Yellowknife Bay, Gale Crater, Mars *Am. Minralogist* **100** 824–36

[19] Pearson V, Sephton M, Kearsley A, Bland P, Frachni I and Gilmour I 2002 Clay mineral-organic matter relationships in the early solar system *Meteor. Planet. Sci.* **37** 1829–33

[20] Sprague A, Hanna K D, Kozlowski R, Helbert J, Maturilli A, Warell J and Hora J 2009 Spectral emissivity measurements of Mercury's surface indicate Mg- and Ca-rich mineralogy, K-spar, Na-rich plagioclase, rutile, with possible perovskite and garnet *Planet. Space. Sci.* **57** 364–83

[21] Treiman A, Lanzirotti A and Xirouchakis D 2004 Ancient water on asteroid 4 Vesta: evidence from a quartz veinlet in the Serra de Magé eucrite meteorite *Earth Planet. Sci. Lett.* **219** 189–99

[22] Okrusch M and Matthes S 2014 Aufbau und Stoffbestand des Mondes *Mineralogie* (Heidelberg: Springer) pp 537–46

[23] Tulej M, Iakovleva M, Leya I and Wurz P 2011 A miniature mass analyser for *in situ* elemental analysis of planetary material performance studies *Anal. Bioanal. Chem.* **399** 2185–200

[24] Tulej M, Riedo A, Iakovleva M and Wurz P 2012 On applicability of a miniaturized laser ablation time of flight mass spectrometer for trace elements measurements *Int. J. Spectrsc.* **2012** 234949

[25] Riedo A, Meyer S, Heredia B, Neuland M B, Bieler A, Tulej M, Leya I, Iakovleva M, Mezger K and Wurz P 2013 Highly accurate isotope composition measurements by a miniature laser ablation mass spectrometer designed for *in situ* investigations on planetary surfaces *Planet. Space Sci.* **87** 1–13

[26] Grimaudo V, Moreno-García P, Riedo A, Neuland M, Tulej M, Broekmann P and Wurz P 2015 High resolution chemical depth profiling of solid material using a miniature laser ablation/ionization mass spectrometer *Anal. Chem.* **87** 2037–41

[27] Tulej M, Riedo A, Neuland M, Meyer S, Wurz P, Thomas N, Grimaudo V, Moreno-García P, Broekmann P, Neubeck A and Ivarsson M 2014 CAMAM: a miniature laser ablation ionisation mass spectrometer and microscope-camera system for *in situ* investigation of the composition and morphology of extraterrestrial materials *Geost. Geoanal. Res.* **38** 441–66

[28] Becker J 2007 *Inorganic Mass Spectrometry* (New York: Wiley)

[29] Riedo A, Neuland M, Meyer S, Tulej M and Wurz P 2013 Coupling of LMS with a fs-laser ablation ion source: elemental and isotope composition measurements *J. Anal. At. Spectrom.* **28** 1256–69

[30] Zhang B, He M, Hang W and Huang B 2013 Minimizing matrix effect by femtosecond laser ablation and ionization in elemental determination *Anal. Chem.* **85** 4507–11

[31] Neuland M, Meyer S, Mezger K, Riedo A, Tulej M and Wurz P 2014 Probing the Allende meteorite with a miniature laser-ablation mass analyser for space application *Planet. Space Sci.* **101** 196–209

[32] Shaheen M, Gagnon J and Freyer B 2012 Femtosecond (fs) laser coupled with modern ICP-MS instruments provide new and improved potential for *in situ* elemental and isotopic analyses in the geosciences *Chem. Geol.* **330/331** 260–73

[33] Chichkov B, Momma C, Nolte S, von Alvensleben F and Tünnermann A 1996 Femtosecond, picosecond and nanosecond laser ablation of solids *Appl. Phys.* A **63** 109–15

[34] Von der Linde D and Sokolowski-Tinten K 2000 The physical mechanismof short-pulse laser ablation *Appl. Surf. Sci.* **154** 1–10

[35] Von der Linde D, Sokolowski-Tinten K and Bialkowski J 1997 Laser solid interaction in the femtosecondtime regime *Appl. Surf. Sci.* **109/110** 1–10

[36] Kaplan A 1998 Precision ablation processing *Handbook of the EuroLaser Academy* vol 2, 1st edn (London: Chapman and Hall) pp 473–502

[37] Seydoux-Guillaume A, Freydier R, Poitrasson F, d'Abzac F, Wirth R and Datas L 2010 Dominance of mechanically over thermally induced damage during femtosecond laser ablation of monazite *Eur. J. Mineral.* **22** 235–44

[38] Zhang S, Zhang B, Hang W and Huang B 2015 Chemometrics and theoretical approaches for evaluation of matrix effect in laser ablation and ionization of metal samples *Spectrochim. Acta* B **107** 17–24

[39] Halas S 2006 100 years of work function *Mater. Sci. Poland* **24** 951–68

[40] Gray H 1965 Orbital ionization energies *Electrons and Chemical Bonding* 2nd edn (New York: Benjamin) pp 217–8 (Tab. A1)

[41] deB Darwent B 1970 Bond dissociation energies in simple molecules *Natl Stand. Ref. Data Ser.,* (Washington, DC: US National Bureau of Standards) **31** 52

[42] Huang R, Yu Q, Tong Q, Hang W, He J and Huang B 2009 Influence of wavelength, irradiance, and the buffer gas pressure on high irradiance laser ablation and ionization source coupled with an orthogonal time of flight mass spectrometer *Spectrochim. Acta* B **64** 255–61

[43] Poitrasson F, Mao X, Freydier R and Russo R E 2003 Comparison of ultraviolet femtosecond and nanosecond laser ablation inductively coupled plasma mass spectrometry in glass, monazite, and zircon *Anal. Chem.* **75** 6184–90

[44] Koch J and Günther D 2007 Femtosecond laser ablation inductively coupled plasma mass spectrometry: achievements and remaining problems *Anal. Bioanal. Chem.* **387** 149–53

[45] Gertsvolf M, Jean-Ruel H, Rajeev P P, Klug D D, Rayner D M and Corkum P B 2008 Orientation-dependent multiphoton ionization in wide band gap crystals *Phys. Rev. Lett.* **101** 243001

[46] Schultz L, Tourtelot H and Flanagan F 1976 Cody Shale SCo-l, from Natrona County, Wyoming *Descriptions and Analyses of Eight New USGS Rock Standards* Geological Survey Professional Paper 840 pp 21–3

[47] Wenk H-R and Bulakh A 2014 *Minerals – Their Constitutions and Origin* (Cambridge: Cambridge University Press)

[48] Hosterman J, Flanagan F, Bragg A, Doughten M, Filby R, Grimm C, Mee J, Potts P and Rogers N 1987 Mineralogy and Instrumental Neutron Activation Analysis of Seven National Bureau of Standards and Three Instituto de Pesquisas Tecnológicas Clay Reference Samples *US Geological Survey*

[49] Huang R, Yu Q, Li L, Lin Y, Hang W, He J and Huang B 2011 High irradiance laser ionization orthogonal time-of-flight mass spectrometry: a versatile tool for solid analysis *Mass Spectrom. Rev.* **30** 1256–68

[50] Freydier R, Candaudap F, Poitrasson F, Arbout A, Chatel B and Dupré B 2008 Evaluation of infrared femtosecond laser ablation for the analysis of geomaterials by ICP-MS *J. Anal. At. Spectrom.* **23** 702–10

[51] Liu C, Mao X, Zeng X, Greif R and Russo R 2004 Nanosecond and femtosecond laser ablation of brass: particulate and ICOMS measurements *Anal. Chem.* **76** 379–83

[52] Tulej M, Neubeck A, Ivarsson M, Neuland M, Meyer S and Wurz P 2015 Chemical composition of micrometer-sized filaments in an aragonite host by a miniature laser ablation/ionization mass spectrometer *Astrobiology* **15** 669–82

[53] online: Barthelmy D, http://webmineral.com/ (accessed 3 August 2015)

[54] Halas S and Durakiewicz T 1998 Work functions of elements expressed in terms of the Fermi energy and the density of free electrons *J. Phys.: Condens. Matter* **10** 10815–26

[55] Li X, Rong W, Jian L, Zhang K, Li C, Cao Q, Zhang G and Lu Y 2014 Generation and elimination of polarization-dependent ablation of cubic crystals by femtosecond laser radiation *Opt. Express* **22** 30170–6

[56] Keller W 1968 Flint clay and flint-clay facies *Clays and Clay Miner.* **16** 113–28

[57] Rohner U, Whitby J A and Wurz P 2004 Highly miniaturized laser ablation time-of-flight mass spectrometer for a planetary rover *Rev. Sci. Instrum.* **75** 1314–22

[58] Mehner E, Bernard B, Giessen H, Kopf D and Braun B 2014 Sub-20 ps pulses from a passively Q-switched microchip laser at 1 MHz repetition rate *Opt. Lett.* **39** 2940–3

[59] Wang S, Wang Y, Yang X, Feng G and Zhou S 2015 High-efficiency microchip laser with self-injection seeding *Appl. Opt.* **54** 10304–8